metals

MDPI

Article

Kinetics Study on the Hydrogen Reduction of Bauxite Residue-Calcite Sintered Pellets at Elevated Temperature

Manish Kumar Kar [1,*], Casper van der Eijk [2] and Jafar Safarian [1]

[1] Department of Materials Science and Engineering, Norwegian University of Science and Technology, Alfred Getz Vei 2, 7491 Trondheim, Norway
[2] SINTEF Industry, Torgarden, 7465 Trondheim, Norway
* Correspondence: manish.k.kar@ntnu.no

Abstract: In this study, the isothermal reduction of bauxite residue-calcite sintered pellets by hydrogen at elevated temperatures and different gas flow rates was investigated. A thermogravimetric technique was applied to study the kinetics of the direct reduction by H_2 at 500–1000 °C. It was observed that iron in sintered oxide pellets mainly exists in the form of brownmillerite, srebrodolskite and fayalite. The reduction of brownmillerite, the dominant Fe-containing phase, with hydrogen produces mayenite, calcite and metallic iron. X-ray diffraction (XRD), scanning electron microscopy (SEM), X-ray fluorescence (XRF), BET surface area, pycnometer and mercury intrusion porosimeter analyses were adopted on reduced pellets to interpret the experimental results. The order of the reduction process changes from first-order reaction kinetics to second-order with an increasing reduction temperature. The change in reaction order may be due to sintering at higher reduction temperatures and corresponding physical and microstructural changes in pellets. The activation energy of reduction was calculated as 55.1–96.6 kJ/mol based on the experimental conditions and using different kinetic model equations. From the experimental observations, it was found that 1000 °C with 60 min is the most suitable condition for bauxite residue-CaO sintered pellets' reduction with hydrogen.

Keywords: isothermal reduction; activation energy; thermogravimetric; first order; second order; kinetics

Citation: Kar, M.K.; Eijk, C.v.d.; Safarian, J. Kinetics Study on the Hydrogen Reduction of Bauxite Residue-Calcite Sintered Pellets at Elevated Temperature. *Metals* **2023**, *13*, 644. https://doi.org/10.3390/met13040644

Academic Editors: Chenguang Bai and Pasquale Cavaliere

Received: 18 February 2023
Revised: 14 March 2023
Accepted: 21 March 2023
Published: 23 March 2023

1. Introduction

The smelter-grade alumina for aluminum production is mainly produced by the Bayer process. Nearly the entire aluminum industry worldwide has adopted the Bayer process for alumina production from bauxite ore [1]. This process generates nearly 1.0 to 1.5 tons of red mud or bauxite residue (BR) as a byproduct per ton of alumina produced, which may vary depending on the geographic region of the ore and the efficiency of processing parameters in the Bayer process [2–4]. BR is partially dewatered red mud and is highly hazardous due to its high alkalinity, fine particle size and heavy metal content. The handling and storing of BR at the industrial scale is a challenging task [5]. Due to its high-volume generation, BR storage will require a large area of land. BR typically contains iron, aluminum, silicon, titanium and several other oxides, and iron and aluminum oxides are the major fractions, with 50 to 70 wt.% of the residue [6,7]. Strict regulations from the European mine directives and European waste legislation significantly limit the landfill disposal of waste and have forced the industry to explore alternative sustainable solutions for this waste [8,9]. Despite many R&D projects, industrial-scale application and economical metal recovery from BR is still anticipated [10,11].

Most iron and steel production is achieved using the blast furnace–basic oxygen furnace (BF-BOF) route, which employs the burning of fossil fuels and generates around 1.9 tons of CO_2 per ton of steel produced [12]. It was estimated that nearly 30% of the industrial emissions and 7% of the total global CO_2 emissions [13] came from the iron

and steel industry alone. Due to increasing concerns about global warming, steel producers have started to turn towards hydrogen reduction as a more sustainable means of production[14–16]. According to the Paris agreement, 45% of CO_2 emissions should be reduced by 2030 and net zero should be achieved by 2050 [17]. This means that replacing fossil fuels with hydrogen as the main reductant will be an appropriate path towards sustainable iron production. During direct reduction with hydrogen, iron oxides are reduced to metallic iron without undergoing a liquid phase and it only generates water vapor as a product gas. Since the reduction of iron oxides using hydrogen is endothermic, energy must be supplied to the process [18]. The energy consumption per ton of liquid steel produced through hydrogen reduction by the direct reduction–electric arc furnace (DR-EAF) route is around 3.72 MWh, slightly higher than the BF-BOF route, which is around 3.48 MWh, without considering the pelletizing and finishing processes for both [19]. The reduction of hematite to metallic iron requires two or three reaction mechanism steps based on the reduction temperature [20]. These reduction equations are described as follows.

At a temperature above 570 °C, a three-stage mechanism is followed:

$$3Fe_2O_3 + H_2 \rightarrow 2Fe_3O_4 + H_2O \quad (1)$$

$$2Fe_3O_4 + 2H_2 \rightarrow 6FeO + 2H_2O \quad (2)$$

$$6FeO + 6H_2 \rightarrow 6Fe + 6H_2O \quad (3)$$

At a temperature below 570 °C, a two-stage mechanism is followed:

$$3Fe_2O_3 + H_2 \rightarrow 2Fe_3O_4 + H_2O \quad (4)$$

$$2Fe_3O_4 + 8H_2 \rightarrow 6Fe + 8H_2O \quad (5)$$

Initially, these reactions were suggested to be strongly dependent on the temperature [20]. In actual practice, it depends upon many parameters, such as internal diffusion resistance, external diffusion resistance, the reaction rate, etc. [21].

The use of BR as a secondary raw material for iron and alumina recovery will accompany the direct use of valuable materials and the valorization of industrial waste towards a circular economy. A sustainable process has been introduced by the HARARE EU project to extract iron, alumina and REEs from BR, and hydrogen reduction has been conducted to reduce iron oxide to metallic iron, followed by the magnetic separation of iron and other metals' recovery. This work falls within the Ca route of the HARARE project, in which BR and calcite-agglomerated pellets are reduced by hydrogen with varying temperatures (isothermally) and H_2 flow rates. The optimized parameters of BR and calcite agglomeration have been studied in our previous work [22]. The purpose of using calcite with BR to form a calcium aluminate phase during hydrogen reduction is that it can be separated by alkaline leaching using sodium carbonate solutions. The present experimental work mainly focuses on understanding the reduction behavior, activation energy calculation and phase transformation of the reduced optimized BR-calcite sintered pellets. In practice, the rate of reduction and the activation energy are important for process design, and they are directly related to the production rate and optimizing the process parameters. Therefore, we tried to extract these fundamental data for the newly produced pellets. Most of the previous studies on the hydrogen reduction of iron oxides have been on hematite and magnetite reduction; however, the novelty of the present work is that the reduction behavior of pellets containing iron complexes of brownmillerite, serbrodolskite and fayalite, which formed during the sintering of BR and calcite pellets, are studied. No similar research work has been performed previously.

2. Materials and Methods

In this section, the materials, methods of characterization and application of hydrogen gas for the reduction of iron complexes in BR-calcite sintered pellets are described.

2.1. Materials

BR was supplied by Mytilineos Metallurgy Business Unit S.A., which was previously named Aluminium of Greece. Limestone (LS) was provided by Omya (Molde, Norway). As-received lumpy materials were dried in an oven at 80 °C overnight and deagglomerated into fine sizes below 500 µm. BR and $CaCO_3$ fine particles were then mixed in a ratio of CaO/Al_2O_3 = 1 using a ball mill for homogenization and were pelletized with a disc pelletizer with ca. 10 wt.% water addition. Resulting green pellets were dried overnight in an oven at a temperature of 110 ± 5 °C. Dried pellets were subsequently sintered in a muffle furnace at 1150 ± 10 °C in air for 120 min [22]. In this paper, RH3, RH5 and RH8 denote sinter pellets reduced at 1000 °C, 800 °C and 500 °C, respectively.

2.2. Direct Reduction

The heating profile for the direct reduction experiment is represented in Figure 1. Heating was carried out in an argon atmosphere with a flow rate of 1 NL/min up to the targeted temperature at a heating rate of 10 °C/min. Initial reduction experiments were performed through the varying flow rate of hydrogen with a constant reduction time and temperature to determine the hydrogen flow rate effect. Afterward, the flow rate was fixed for all the reduction experiments between 500 °C and 1000 °C with 100 °C intervals, but it was performed with different reduction times. Cooling was carried out under argon flow to prevent iron reoxidation upon cooling.

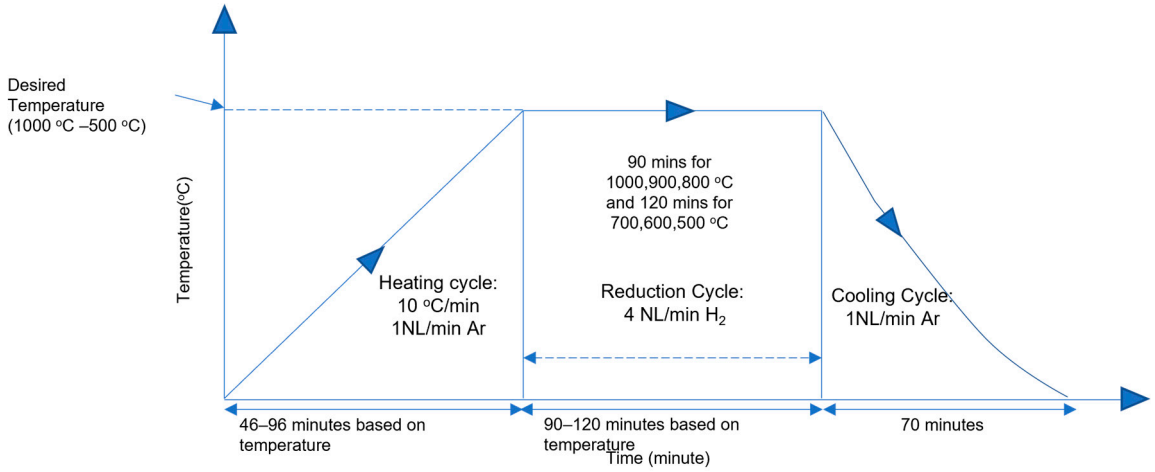

Figure 1. Heating profile of reduction experiments.

The direct reduction of pellets was conducted isothermally under a hydrogen atmosphere in a thermogravimetric (TG) furnace (ENTECH, Angelholm, Sweden). A schematic view of the TG furnace is shown in Figure 2. A schematic of the crucible is shown in Figure 2A, and the overall setup of the furnace is shown in Figure 2B. The shape of the crucible was a hollow cylinder, and the sample was placed at the bottom and inside the crucible on a steel grid with a porous alumina plug that maintained a uniform gas flow. A thermocouple was inserted in the middle of the crucible and placed at the halfway point of the sample height, as shown in Figure 2A. There were two thermocouples in the furnace; one was located on the furnace wall, and other was in the middle of the sample. The inert or hydrogen gas was introduced from the top of the crucible into the outer part of the crucible, and after being preheated, it was introduced to the bottom of the sample bed, and it flowed out through the top of the inner part of the crucible to the off-gas line. The target temperature was set based on the thermocouple temperature reading. The crucible

was hung in a weight balance, and the weight loss data were transferred directly to a data logging system. The logging system was connected to a gas flow controller device, weighing balance, temperature controller and outgas analysis system. To study the flow rate of H_2's effect on direct reduction, we reduced the sample at 1000 °C for 90 min using 2 NL/min, 3 NL/min and 4 NL/min flow rates, and 4 NL/min was chosen for the other experiments based on providing the highest rate of reduction. Subsequent experiments were conducted at a 4 NL/min H_2 flow rate with a varying reduction time and temperature. For reductions at 1000 °C, 900 °C and 800 °C, the reduction time was 90 min; meanwhile, for reductions at 700 °C, 600 °C and 500 °C, the time was set at 120 min. The reduction time for the lower-temperature reductions was longer to compensate for the lower reduction kinetics. For each test, we used approximately 50 g of sample.

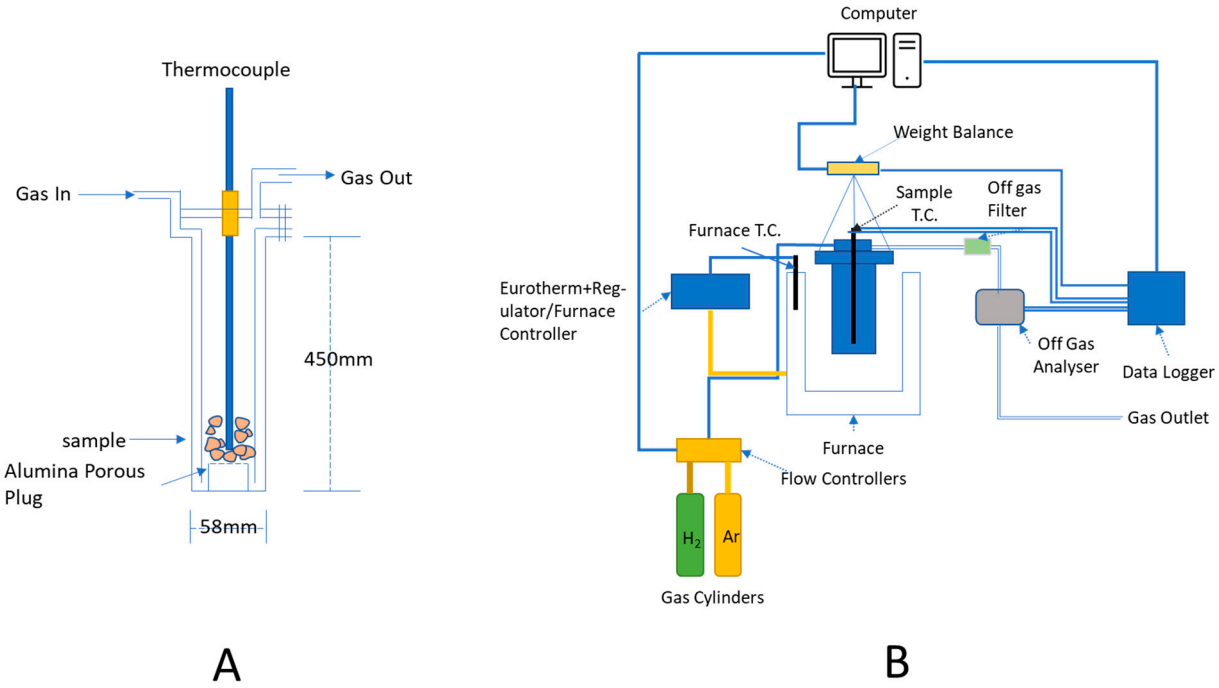

Figure 2. Schematic of thermogravimetric furnace setup, crucible (**A**) overall set up furnace (**B**).

2.3. Methods for Characterization

Mineralogical phase analysis of raw materials sintered and reduced pellets were conducted with the X-ray diffraction (XRD) technique using the Bruker D8 A25 DaVinciTM, Karlsruhe, Germany, with CuKα radiation (wavelength λ of 1.54 Å), a 2θ range from 15 to 75 and a step size of 0.03°. Qualitative results were analyzed using the EVA diffraction software with a crystallographic database. Elemental analysis of pellets was performed using the X-ray fluorescence (XRF) technique with a device from Thermo Fisher, Degerfors, Sweden. Sample preparation of testing in XRF was performed by using the flux fusion method. Microstructural examination of the products was performed via a Field Emission Scanning Electron Microscope (Zeiss Ultra FESEM, National Institute of Standards and Technology, Gaithersburg, MD, USA) equipped with an XFlash® 4010 Detector supplied by the Bruker Corporation (Billerica, MA, USA) for Energy-Dispersive X-Ray Spectroscopy (EDS). EDS analysis was employed for the elemental analysis of different regions in the sample. The porosity and pore size distribution of pellets were measured using a mercury intrusion porosimeter, Autopore IV 9520, Micropolitics, (Micromeritics Instrument Corporation, Norcross, GA, USA). The density of reduced pellets was measured using a Pycnometer, Micromeritics and Accupyc 1350, with helium gas of 99.99% purity. The BET surface area was measured using a 3Flex 3500 Chemisorption Analyzer, Micromeritics (Micromeritics Instrument Corporation, Norcross, GA, USA). Before the BET area mea-

surement, the sample was degassed at 250 °C for 10 h to remove the moisture content of sintered pellets before the BET analysis.

3. Results

The obtained results from the experiments are presented below.

3.1. Characterization of Materials

The results of XRF analysis for the dried, sintered and reduced pellets are listed in Table 1. As the dry pellet sample had $CaCO_3$ during the sintering of the dry pellets, all $CaCO_3$ was decomposed to CaO and CO_2, which led to loss on ignition. However, for sintered and reduced pellets, there was very low LOI. The XRF gave the results in elemental form, and as all-iron complexes were reduced to metallic iron as per XRD, we normalized and recalculated them in the form of Fe. For the sintered oxide pellets, all iron oxides were assumed in the form of Fe_2O_3 in different compounds, such as brownmillerite and srebrodolskite. The XRF results of sintered pellets showed that the weight percentages of most oxides increased due to sintering, but the Na_2O and MgO content decreased. In addition, the Na_2O content also decreased due to reduction. The metallic iron content of the completely reduced sample at 1000 °C was around 21.4%.

Table 1. XRF analysis of dried, sintered and reduced pellets.

Sample/Oxides	RM + $CaCO_3$ (C_1A, Dried)	Sintered (1150 °C, C_1A)	Reduced RH3 (1000 °C)
Al_2O_3	13.20	19.80	23.60
CaO	27.50	32.80	35.90
Fe_2O_3/Fe	23.20	29.60	21.40 (Fe)
K_2O	0.15	0.19	0.09
MnO	0.04	0.05	0.05
MgO	0.59	0.51	0.87
Na_2O	2.55	2.31	2.22
P_2O_5	0.07	0.12	0.10
SO_3	0.58	0.96	0.86
SiO_2	6.05	8.30	9.75
TiO_2	3.25	4.07	4.39
Cr_2O_3	0.14	0.20	0.20
V_2O_5	0.11	0.15	0.13
NiO	0.07	0.10	0.06
LOI	22.40	0.72	0.24

XRD of the raw materials is presented in Figure 3. As shown in the XRD plot, the major fraction of BR is composed of hematite (Fe_2O_3) and diaspore ($AlHO_2$). In addition, it also contains cancrinite ($C_{0.7}H_{1.7}Al_3Ca_{0.75}Na_3O_{12.4}Si_3$), katoite ($AlCa_3H_{9.7}O_{12}Si_{0.69}$), perovskite ($CaTiO_3$), anatase ($TiO_2$), coesite ($SiO_2$), goethite (FeOOH), sodalite ($Al_3ClNa_4O_{12}Si_3$) and calcite ($CaCO_3$). Meanwhile, the limestone mainly consists of the $CaCO_3$ phase, and the minor phases are not detected due to significant X-ray diffraction from calcite. The phases of the sintered pellets are presented in Figure 3.

3.2. Reduction Rate under Different Conditions

3.2.1. Effect of Gas Flow Rate

The mass loss changes with time for reduction at 1000 °C for 90 min with varying H_2 flow rates (2 NL/min, 3 NL/min and 4 NL/min) are shown in Figure 4. The relative total mass loss was almost equal for all three different flow rates; however, the initial rate of mass loss increased slightly at 4 NL/min. The mass loss was less for 2 NL/min as compared to 3 NL/min and 4 NL/min. The shape of the curves in Figure 4 indicates that reduction was almost completed for all flow rates after 60 min of reduction time.

3.2.2. Effect of Temperature

Figure 5 shows the reduction curves for reduction at different temperatures under a constant hydrogen flow rate, and obviously the mass loss increases with increasing

temperature at each reduction time. Regarding the same sample masses before reduction, the extent of mass change shows that the reduction was incomplete for lower reduction temperatures within 2 h, since the mass loss curves at 500–700 °C were not leveled off. The maximum weight loss of ~11.5% was found at 1000 °C, which is approximately the theoretical weight loss that will be presented in Section 4.3.

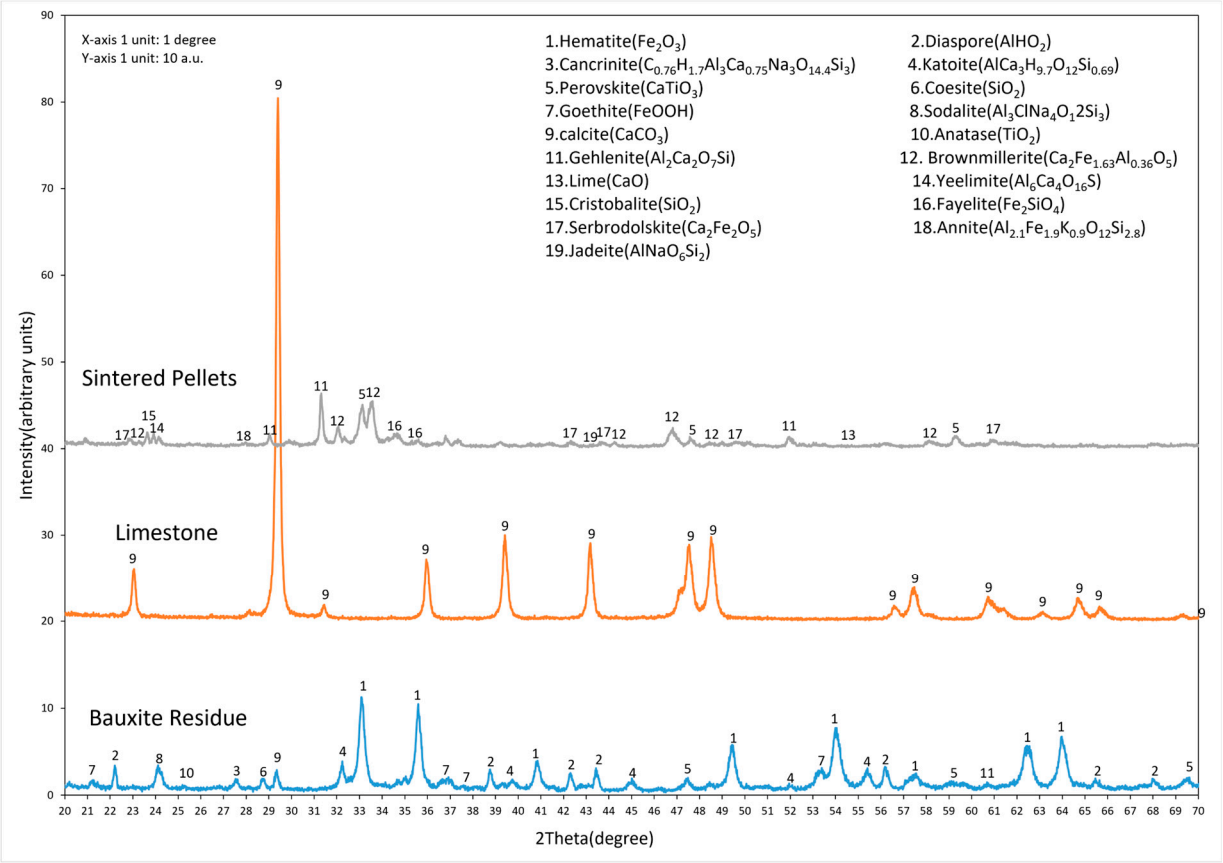

Figure 3. XRD analysis of bauxite residue, limestone and sintered pellets.

3.3. Physical Properties of Pellets

The overall mass losses of the samples correlate with both the change in the gas flow rate and the reduction temperature, as observed in Figures 4 and 5. However, the correlation between the mass loss and gas flow rate is much smaller than that between the mass loss and reduction temperature. The mass loss of the sample increased only by approximately 0.4% (11.1% to 11.5%) when the gas flow rate was increased two-fold (2 NL/min to 4 NL/min). To evaluate this better, the changes in mass loss at different reduction temperatures with a fixed flow rate of 4 NL/min are shown in Figure 6. The mass loss percentage at a 500 °C reduction temperature was around 3.1% and was raised to 11.5% at a 1000 °C reduction temperature, with almost a linear relationship. However, the mass changes with a temperature change from 900 to 1000 °C were insignificant.

The BET surface area of the sample reduced at 1000 °C was approximately 1.0044 m^2/g (Figure 7), while those for the samples reduced at 800 °C and 500 °C were 1.3229 m^2/g and 1.2994 m^2/g, respectively. The relationship between the reduced pellet porosity and BET surface area and the reduction temperature is as shown in Figure 7. The porosity of the sample reduced at 500 °C was around 54.2%, and it increased slightly for the 800 °C reduced sample, and then decreased with reduction at 1000 °C to approximately 51.7%. The change in porosity between 500 and 1000 °C is not significant; however, the BET surface area and porosity of the reduced pellets show related trends, as in Figure 7.

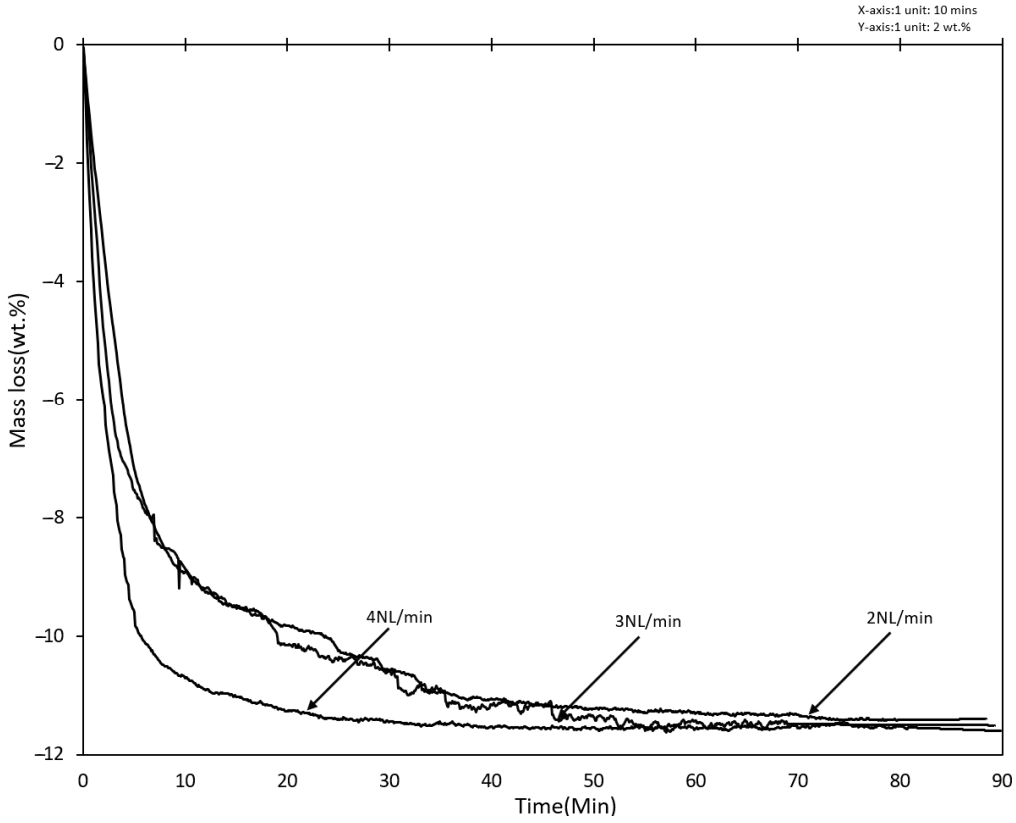

Figure 4. Mass loss plotted against time for different flow rates at constant temperature of 1000 °C.

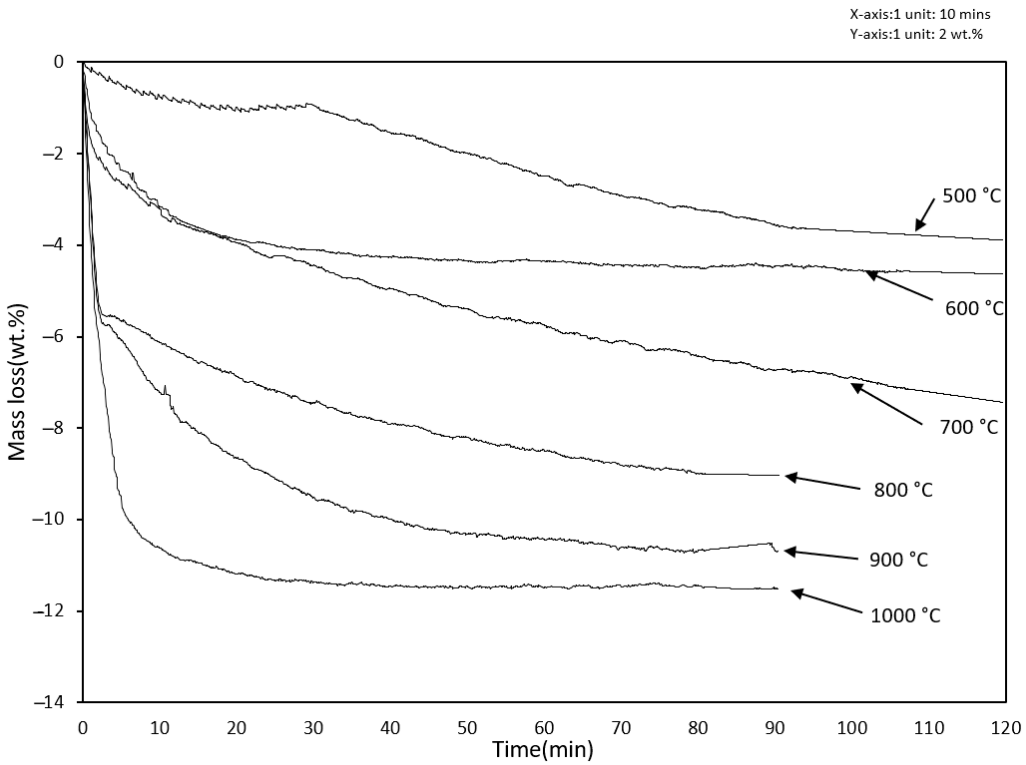

Figure 5. Mass loss changes plotted against time for different temperatures at constant gas flow rate of 4 NL/min.

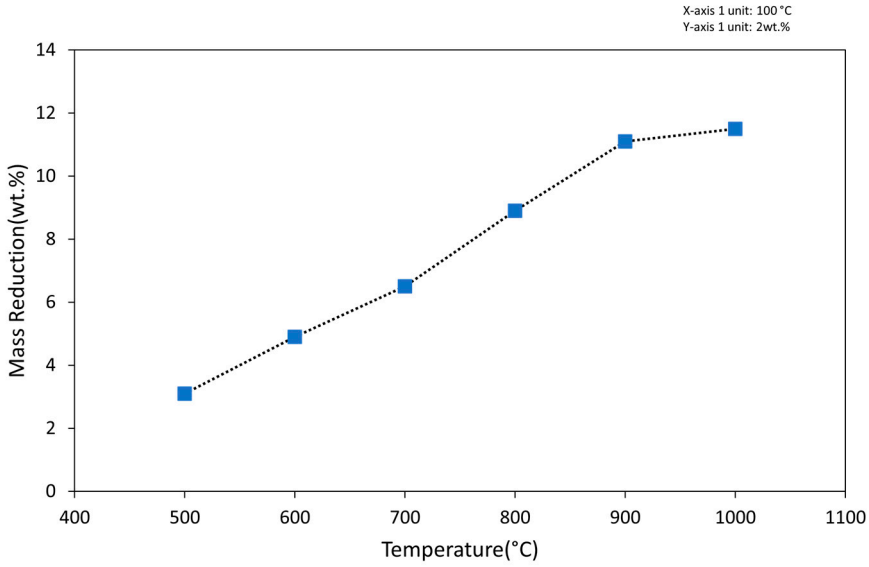

Figure 6. Mass loss against reduction temperature at constant H_2 gas flow rate.

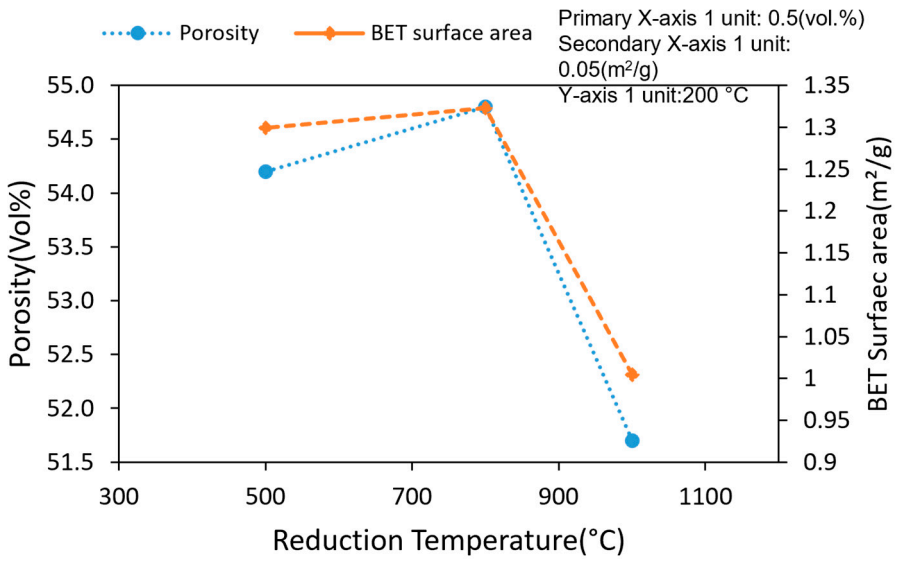

Figure 7. Porosity of reduced pellets at different reduction temperatures.

The true density of pellets reduced at 1000 °C was the highest at around 3.55 g/cm^3; however, the density of the pellets reduced at 800 °C was the lowest and was lower than the ones reduced at 500 °C, as shown in Figure 8. The relationship between density and the reduction temperature was found to be non-linear, as shown in Figure 8, with a V-shaped form.

3.4. Phase Analysis

As shown in Figure 9, the identified phases in samples that were reduced at different flow rates with a constant reduction time and temperature were similar. The major phases of the reduced samples were metallic iron (Fe), perovskite ($CaTiO_3$), lime (CaO), mayenite ($12CaO.7Al_2O_3$), gehlenite ($Ca_2Al_2SiO_7$) and larnite (Ca_2O_4Si). Titanium was found in the form of calcium titanate ($CaTiO_3$) and silica was present as $Ca_2Al_2SiO_7$ and Ca_2SiO_4. A calcium aluminate phase was also found in the reduced sample, which was $Ca_{12}Al_{14}O_{33}$. XRD spectra of the samples reduced at different reduction temperatures were plotted as illustrated with the identified peaks in Figure 10. As we can observe, the peak intensity for metallic iron, lime and mayenite was increased when increasing the reduction temperature.

In contrast, the relative intensities of the gehlenite, perovskite and brownmillerite phases were decreased when increasing the reduction temperature.

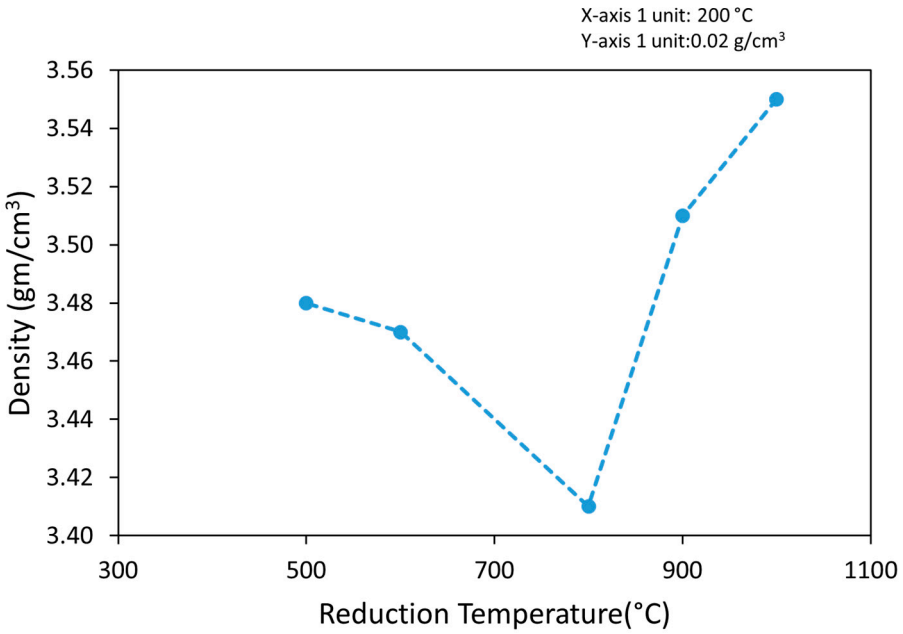

Figure 8. Density of reduced pellets at different reduction temperatures.

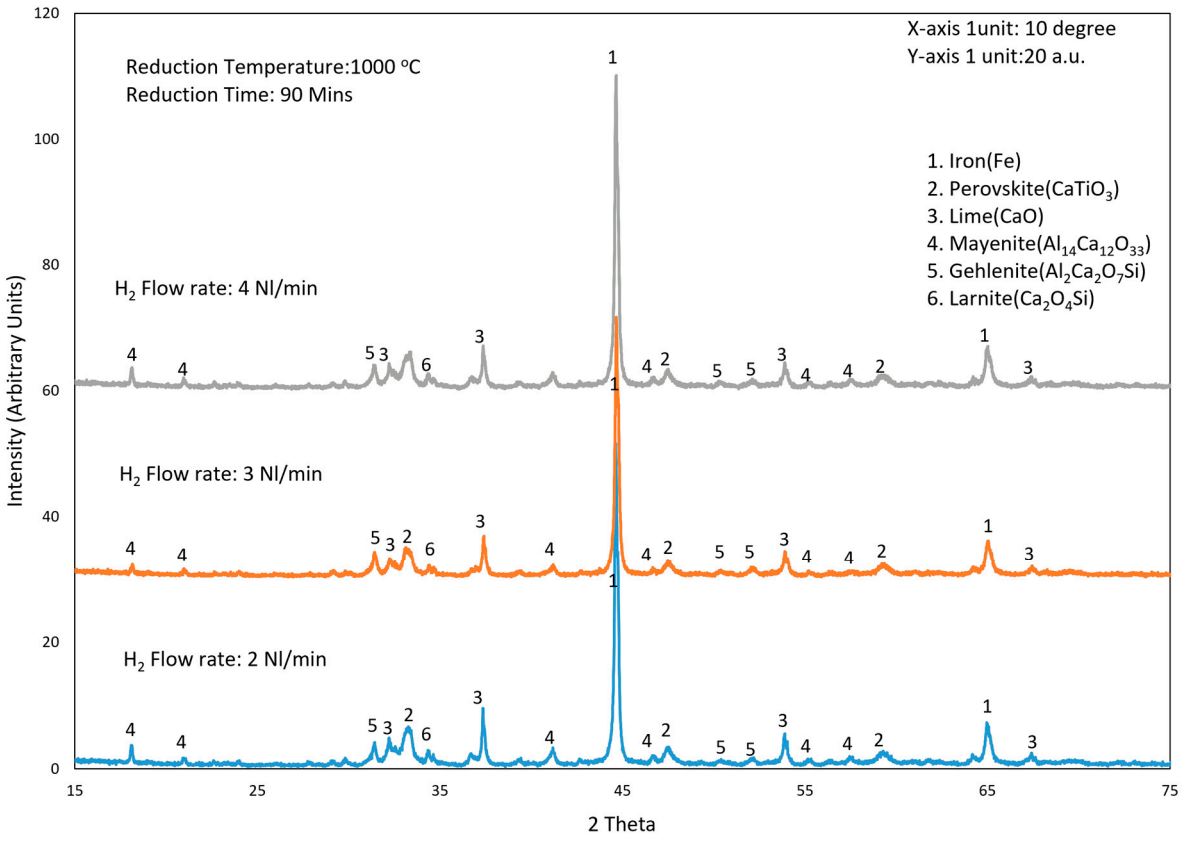

Figure 9. X-ray diffraction analysis of samples reduced at different flow rates of hydrogen with constant reduction time and temperature.

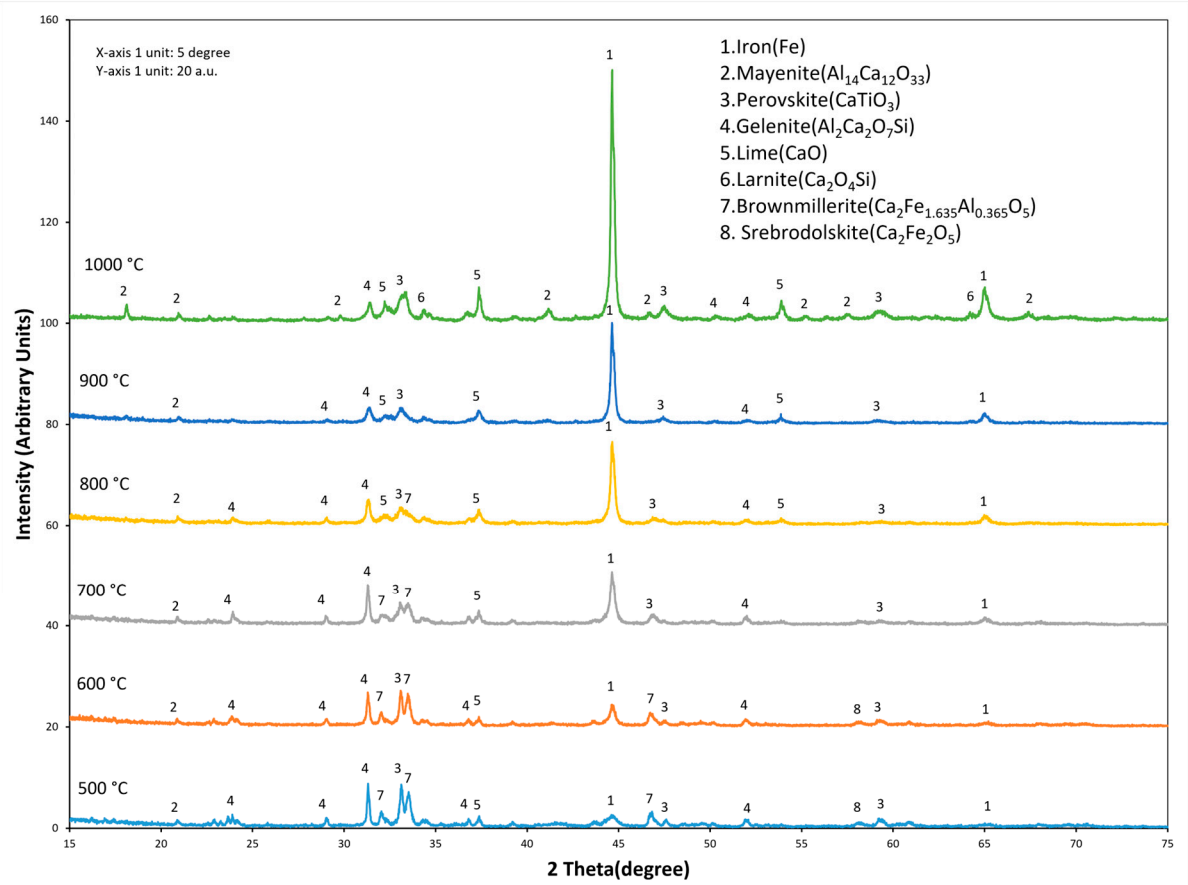

Figure 10. X-ray diffraction analysis of samples reduced at different reduction temperatures with constant hydrogen flow rates.

3.5. Microstructure Analysis

SEM imaging and EDS point analysis were performed for three different reduction temperatures and typical results are presented in Figure 11. Figure 11a shows the microstructure of pellets reduced at 1000 °C, and it shows metallic Fe, the white particles in the image. The whitish-grey phase in the image is $CaTiO_3$, the dark grey area is a mixture of calcium aluminate and sodium aluminate, and the light grey area is gehlenite. Figure 11d shows the microstructure of the 1000 °C reduced sample at lower magnification. EDS elemental mapping analysis of pellets reduced at 1000 °C is presented in Figure 12, which confirms that iron was mainly present as metallic iron, since there was no oxygen overlapping in this area, which was confirmed by point analysis as well. Two other high-intensity areas existing in the sample contain Ca, Ti and O, which were the $CaTiO_3$ phase, and Ca, Al and O, which were the mayenite phase. It was observed on the EDS imaging that in some areas, aluminum combined with sodium, which suggests the existence of a sodium aluminate phase; however, it was not observed in the XRD analysis. Iron in the sample that was reduced at 800 °C was mainly present as a brownmillerite variant ($Ca_2Fe_{1.635}Al_{0.365}O_5$) and metallic iron, as shown by the XRD analysis of the sample (Figure 11c). Other major phases found in the sample reduced at 800 °C were $CaTiO_3$, sodium aluminate and calcium aluminate, and the presence of these phases was confirmed both by EDS elemental mapping analysis (Figure 13) and by XRD analysis (Figure 11c). As shown by the EDS elemental analyses in Figures 13 and 14, most of the iron element was present in combination with oxygen for samples that were reduced at 800 °C and 500 °C. Calcium generally exists in a different area in combination with iron and titanium. One interesting EDS analysis result was in the sample reduced at 800 °C, where sodium

aluminate was found to be encapsulated by calcium titanate and brownmillerite. The EDS elemental mapping indicates that selected elements of interest were widely distributed, and the phases were relatively complex.

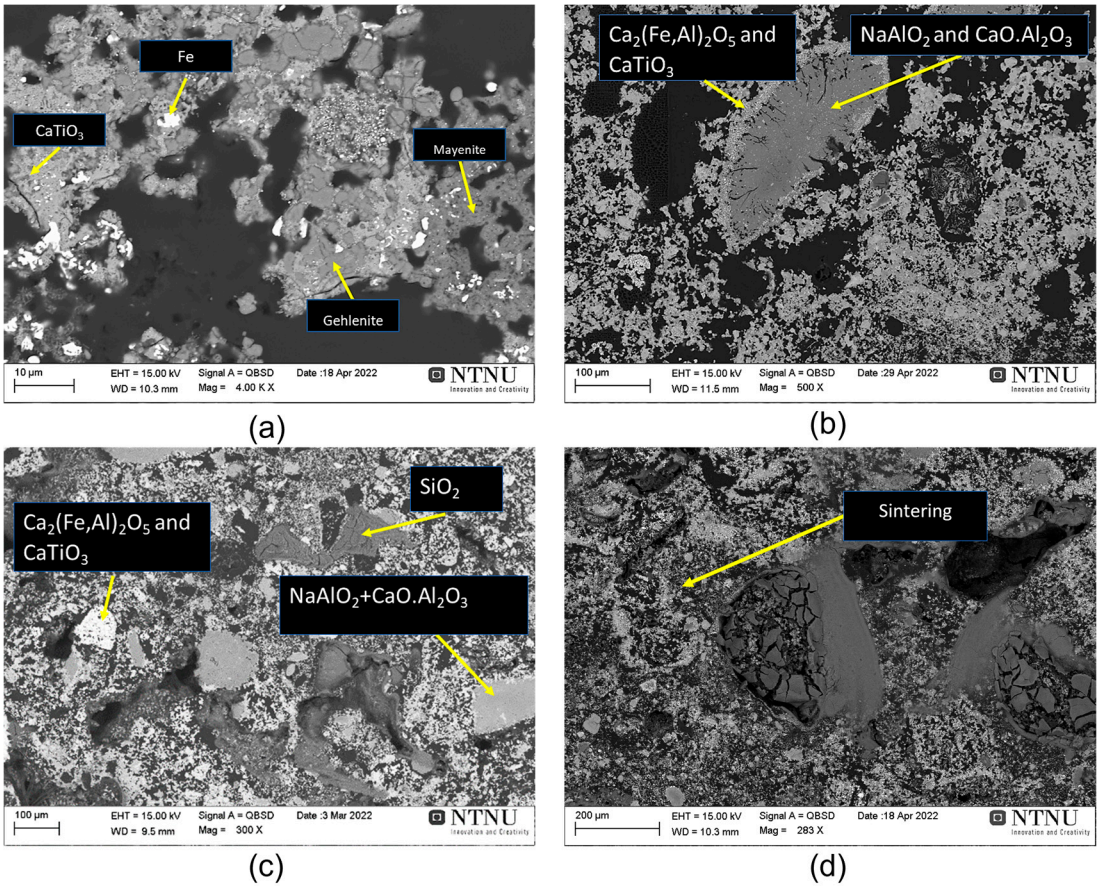

Figure 11. SEM image analysis of reduced pellets at different temperatures: 1000 °C at 4000X (**a**); 800 °C (**b**), 500 °C (**c**) and 1000 °C at 283X (**d**).

The transition of iron complexes with increasing reduction temperature is shown in Figure 15. The dominant iron complex at lower temperatures (500 °C and 800 °C) was brownmillerite; meanwhile, at higher temperature (1000 °C), it was metallic iron. The EDS elemental analysis of iron phases at different reduction temperatures is presented in Table 2. It was discovered that the atomic percentage of iron in the respective complex increases with a higher reduction temperature. At a 1000 °C reduction temperature, iron's atomic % in the complex was nearly 97%. At 800 °C and 500 °C reduction temperatures, iron was present in combination with aluminum, calcium and oxygen, and the atomic percentages of these three elements were higher for samples reduced at 500 °C compared to the ones reduced at 800 °C, as shown in Table 2. Figure 15, for sample (RH5) reduced at 800 °C, shows that the metallic iron complex exists along with the more dominant brownmillerite complex; the existence of both complexes was supported by the XRD results.

Table 2. Comparison of atomic fraction in EDS elemental analysis of RH3, RH5 and RH8.

Sample/Elements (at. %)	Fe	Ca	Al	Si	Ti	O
RH3 (1000 °C)	96.3	2.5	0.6	0.3	0.1	-
RH5 (800 °C)	72.1	10.4	1.2	0.3	3.8	10.2
RH8 (500 °C)	52.7	11.6	4.1	1.5	0.2	28.1

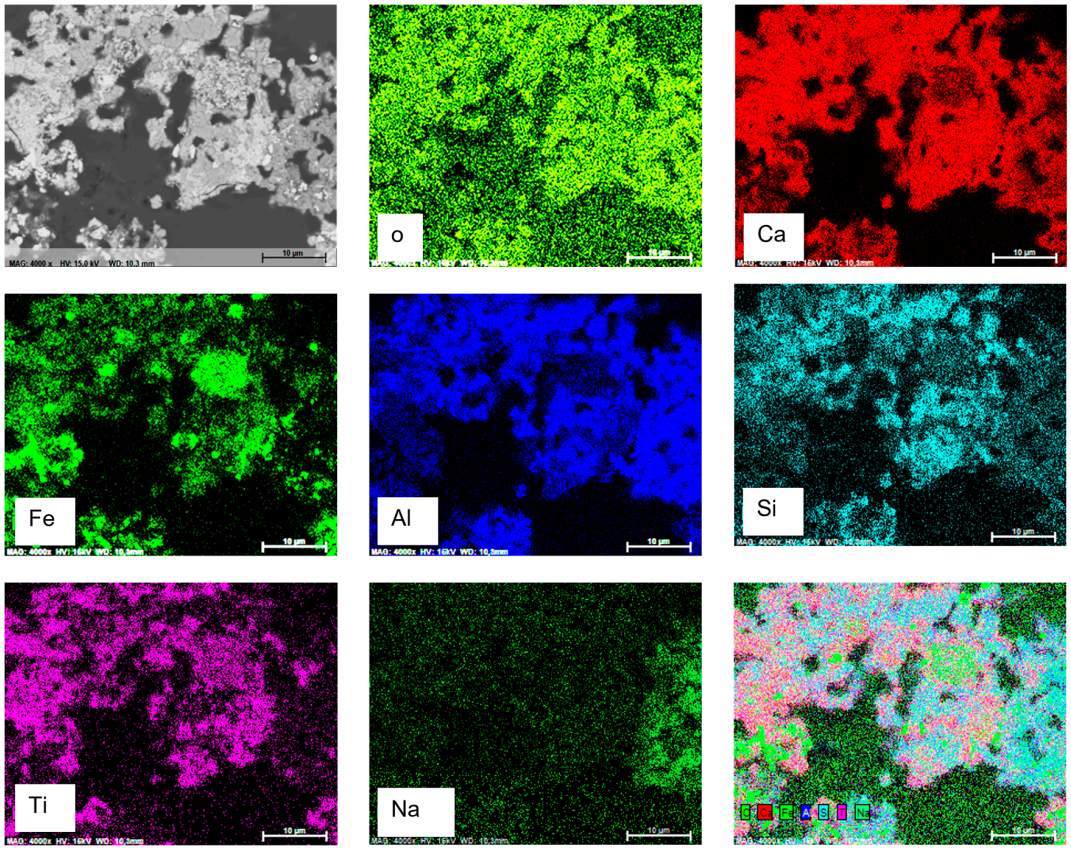

Figure 12. SEM image and EDS analysis of reduced sample RH3.

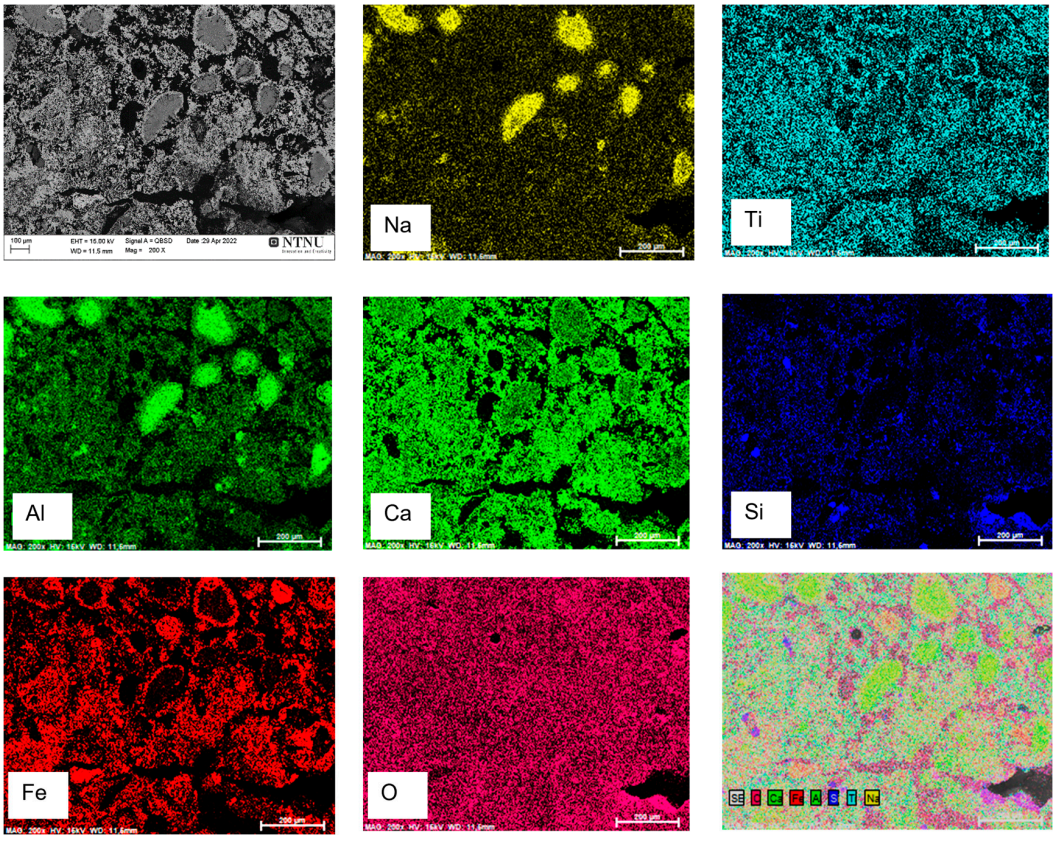

Figure 13. SEM image and EDS analysis of reduced sample RH5.

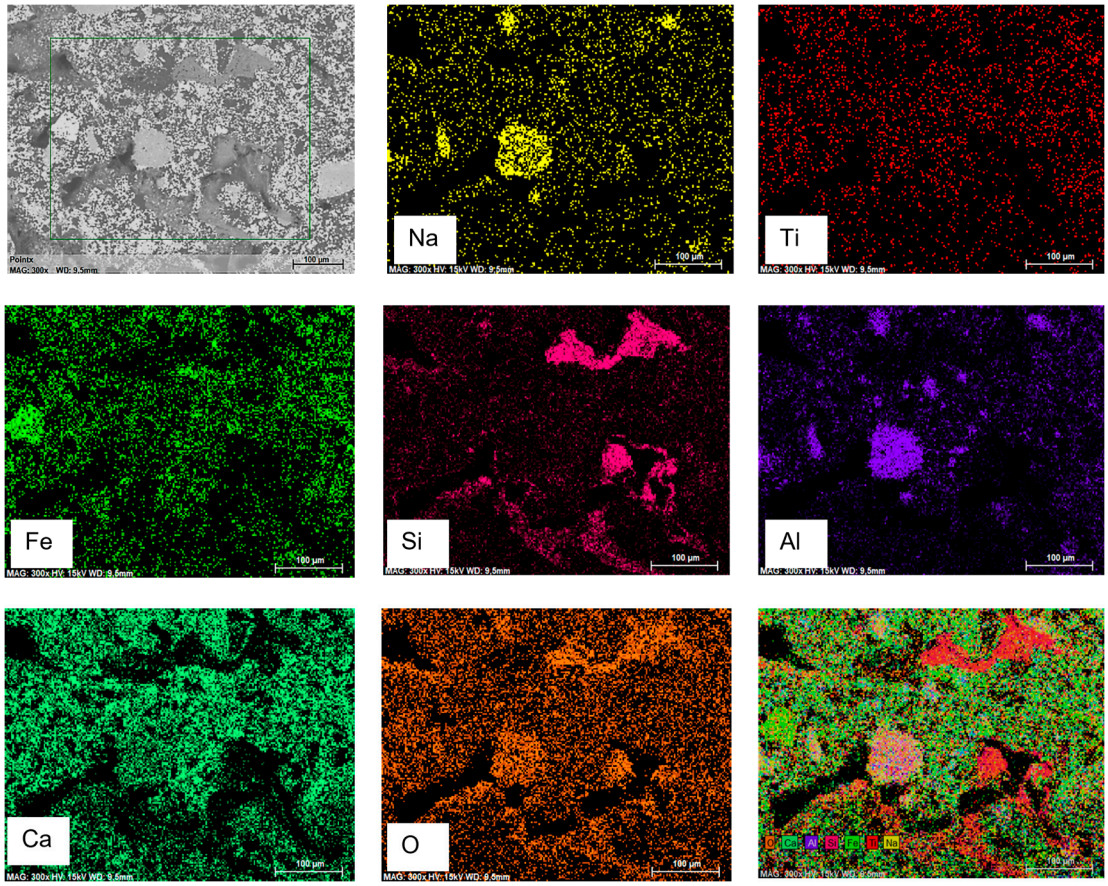

Figure 14. SEM image and EDS analysis of reduced sample RH8.

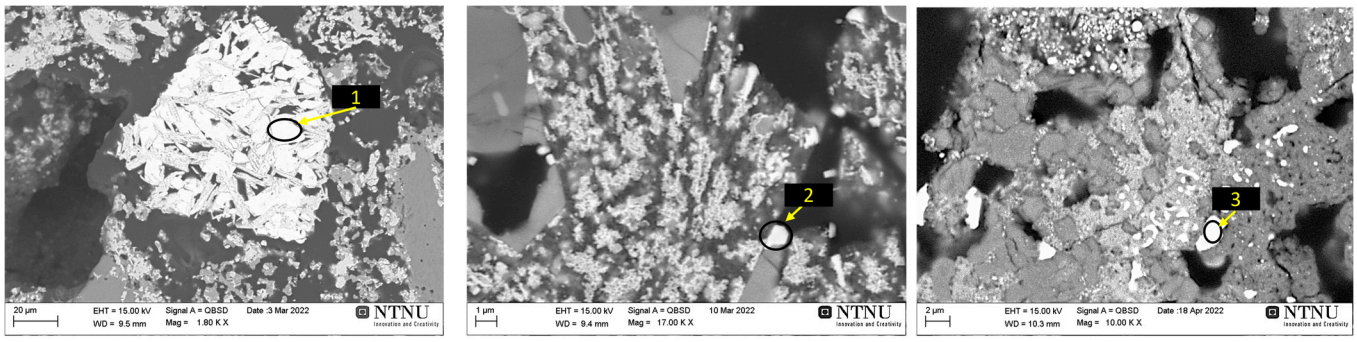

Figure 15. Transition of iron complexes to metallic iron with increasing reduction temperature and elemental of analysis of RH8, RH5 and RH3 are pointed as 1, 2 and 3 respectively.

4. Discussion

4.1. Physical Properties

Porosity measurement was performed regarding the sample weight and volume, and the applied mercury pressure. However, for a given sample volume, the mass loss of the sample reduced at a higher temperature was greater than in the lower-temperature reduced sample due to the larger extent of reduction. Therefore, in the mercury porosimeter, it was found that the porosity increases and again decreases when increasing the reduction temperature, as we did not observe sintering at 800 °C and lower temperatures. However, at a higher reduction temperature than 800 °C, the sintering of the oxide phases/particles occurred, which may cause a loss in porosity. As the reduction temperature increases, more

iron complexes are reduced to metallic iron, accompanied by higher oxygen removal from the pellet, resulting in the sintering of more reduced iron as well.

The true density is calculated by dividing the sample's total weight by the actual volume of the pellet. As shown in Figure 8, the sample reduced at 1000 °C had a higher density than those reduced at 800 °C and 500 °C. As shown by the XRD and EDS analysis, most of the iron complexes in the sample reduced at 1000 °C were converted to metallic iron. Both a volume and weight reduction occurred in samples reduced at 1000 °C due to the sintering of both metallic iron and the non-metallic phases, which is clearly observed in Figure 15. The density of the sample reduced at 500 °C was higher than that reduced at 800 °C. Visual examination showed that a volume reduction did not occur in the samples reduced at 500 °C and 800 °C, while the sample reduced at 800 °C experienced a greater weight reduction than the sample reduced at 500 °C. This discrepancy showed that iron complex reduction in the sample at 800 °C occurred without a volume change, which is indicative of insignificant sintering and higher porosity as compared to 500 °C. The sample reduced at 500 °C had a significantly lower iron complex reduction extent.

4.2. Phase Evolution and Microstructural Analysis

In the sintered pellet, the majority of iron oxide was present in the brownmillerite phase ($Ca_2Fe_{1.632}Al_{0.364}O_5$); however, during reduction, the brownmillerite phase is reduced to metallic iron, mayenite, CaO and water vapor [23]. XRD analysis (Figure 10) showed that the intensity of the iron, CaO and mayenite peaks was increased with the increasing reduction temperature; meanwhile, the brownmillerite peaks' intensities were decreasing and completely disappeared at the highest temperature. The reduction equations of brownmillerite, srebrodolskite and fayalite with hydrogen are as follows:

$$7Ca_2[Fe_x, Al_{1-x}]_2O_5(s) + 21x\ H_2(g) = 14x\ Fe(s) + 21xH_2O(g) + (2 + 12x)CaO(s) + (1 - x)Ca_{12}Al_{14}O_{33}(s) \quad (6)$$

$$Ca_2Fe_2O_5 + H_2 \rightarrow 2Fe + 2CaO + 3H_2O \quad (7)$$

$$Fe_2SiO_4 + 2H_2 \rightarrow 2Fe + SiO_2 + 2H_2O \quad (8)$$

The Gibbs free energy changes in srebrodoliksite ($Ca_2Fe_2O_5$) and fayalite (Fe_2SiO_4) reduction by hydrogen at different reduction temperatures were calculated and are shown in Figure 16. For pure srebrodoliksite and fayalite, whose activities are unified, the change in free energy is negative at a 1000 °C reduction temperature. Thermodynamic calculation shows that the reduction of srebrodolskite and fayalite to metallic iron by hydrogen gas starts below 1000 °C; however, the reduction was started at a lower reduction temperature, as observed by XRD and SEM analysis. This may be because there were many oxide phases in the reduced pellets, and the activity of the product phases becomes less than unity, which drives the reaction to the right. As the product of Reaction (6) has a greater number of phases compared to Reactions (7) and (8), the activity of the product components in Reaction (6) is expected to be lower than in Reactions (7) and (8). This may be the reason that the reduction of brownmillerite starts below the thermodynamic equilibrium temperature as compared to srebrodolskite and fayalite. It is worthwhile to note that the main difference in $Ca_2Fe_2O_5$ with the brownmillerite detected by XRD (Figure 3) is the existence of a small portion of Al in its structure (0.365 moles Al and 1.635 moles Fe), instead of 2 moles Fe in $Ca_2Fe_2O_5$, while the number of moles of Ca is the same. Although the thermodynamic properties of $Ca_2Fe_{1.635}Al_{0.365}O_5$ do not exist in the thermodynamic database, the behavior of $Ca_2Fe_2O_5$ in Figure 16 can be illustrative of the Gibbs energy changes of $Ca_2Fe_{1.635}Al_{0.365}O_5$, and the real line may present a slight difference from that for $Ca_2Fe_2O_5$.

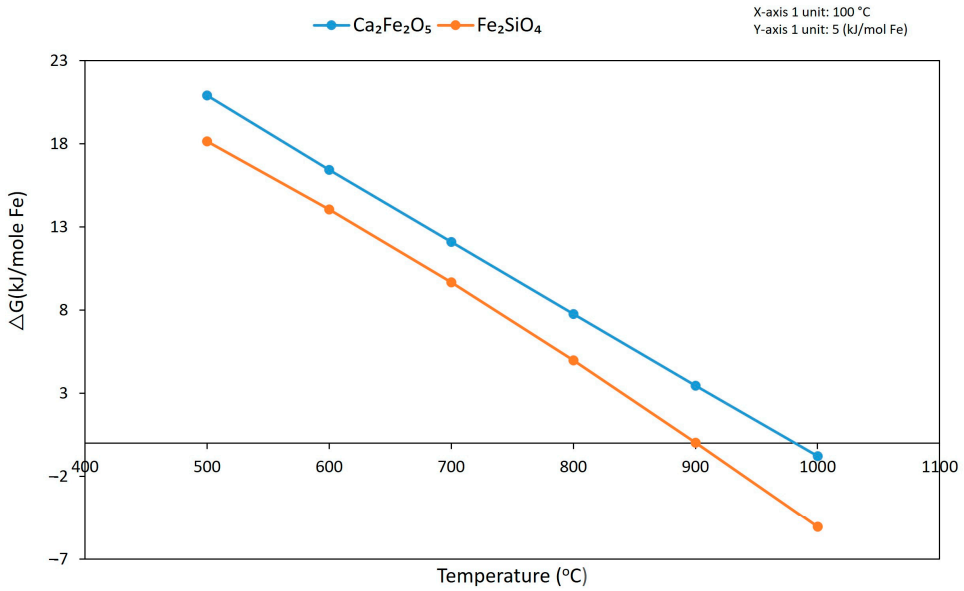

Figure 16. Gibbs free energy changes of Reactions (7) and (8) calculated by Factsage 8.

XRD analysis shows that the CaO intensity increases with the increasing reduction temperature due to the greater reduction of brownmillerite into iron, mayenite, calcium oxide and water vapor; see Reaction (6). At a 1000 °C reduction temperature, the Ca_2SiO_4 phase was found, which might be formed by the interaction of calcite and silica from BR. The formation reaction of Ca_2SiO_4 and its free energy is presented in Equation (9), and obviously its formation is possible at the applied process temperature.

$$2CaO + SiO_2 \rightarrow Ca_2SiO_4\ , \Delta G_{1000^{\circ}C} = -127.6 \frac{kJ}{mol} \quad (9)$$

4.3. Fraction Reduction and Activation Energy Calculation

During the direct reduction of sintered pellets with hydrogen, the rate of weight loss increases with temperature due to the faster reaction kinetics at higher temperatures. This is due to the faster mass transport by diffusion and the more decreased free energy of the reaction, which drives the reaction to the right. The reduction rate also increases with a higher hydrogen flow rate due to the higher volume of hydrogen available for reduction, which subsequently increases the reduction kinetics.

For all experiments, the fractions reduced with time at different temperatures were calculated using Equation (10) and the obtained reduction curves are presented in Figure 17. It was observed that the reduction kinetics at higher temperatures (1000, 900, 800 °C) were significantly higher at the early stage of reduction and decreased as time progressed toward the end of reduction. At low reduction temperatures (700, 600 and 500 °C), the reduction was not completed within the applied duration due to the slower reduction kinetics.

$$X = \frac{\triangle w}{w_{in}} \quad (10)$$

where X is the fraction reduced, Δw is the weight loss during reduction (actual oxygen removed from iron complexes) and w_{in} is the theoretical amount of oxygen present in Fe_2O_3 of the initial mass.

The reduction rate is higher and more extensive for the sample reduced at 1000 °C as compared to lower reduction temperatures. The fraction reduced of iron complexes is close to 0.99 for the sample reduced at 1000 °C, but with a decreasing reduction temperature, it reaches as low as 0.28 for the 500 °C reduced sample. There were some possible errors in the mass readings due to changes in the gas total flow rate, range of particle sizes (4 to

10 mm), high temperature weighing and inhomogeneities along the particles, which were taken into consideration.

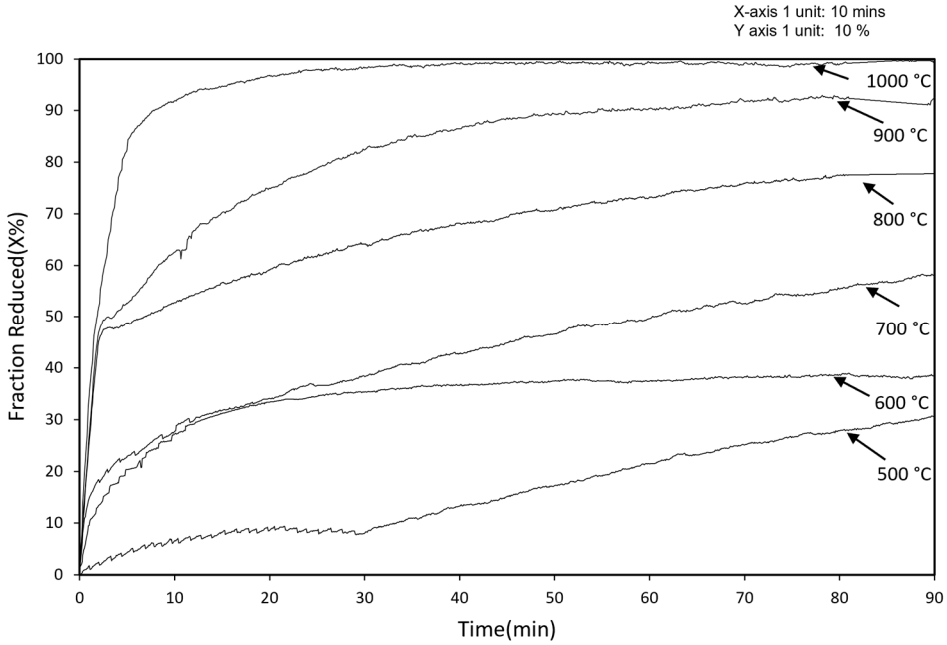

Figure 17. Fraction reduced curves of oxide-sintered pellets with temperature.

To calculate the activation energy, different reaction order models were used for the better fitting of a fraction conversion function, g(α), with time [24]. However, only first- and second-order models (presented in Figures 18 and 19) had a good fit with these results. Based on the first- and second-order reaction models, the activation energy was calculated and is listed in Table 3.

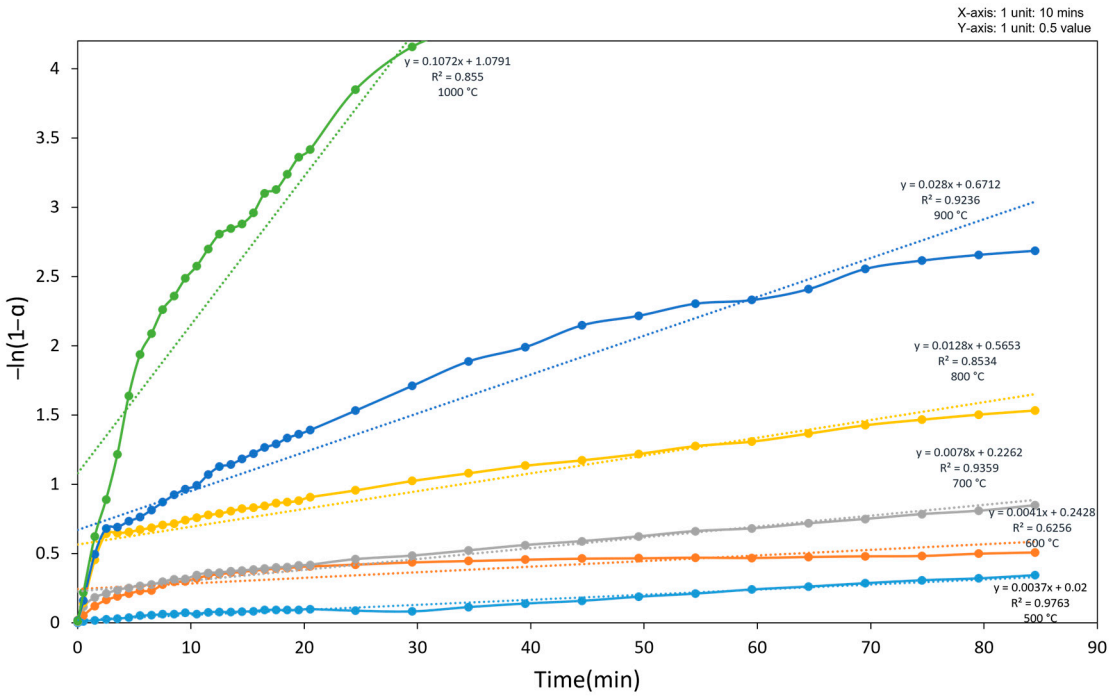

Figure 18. Relation between $-\ln(1-\alpha)$ and time for different reduction temperatures.

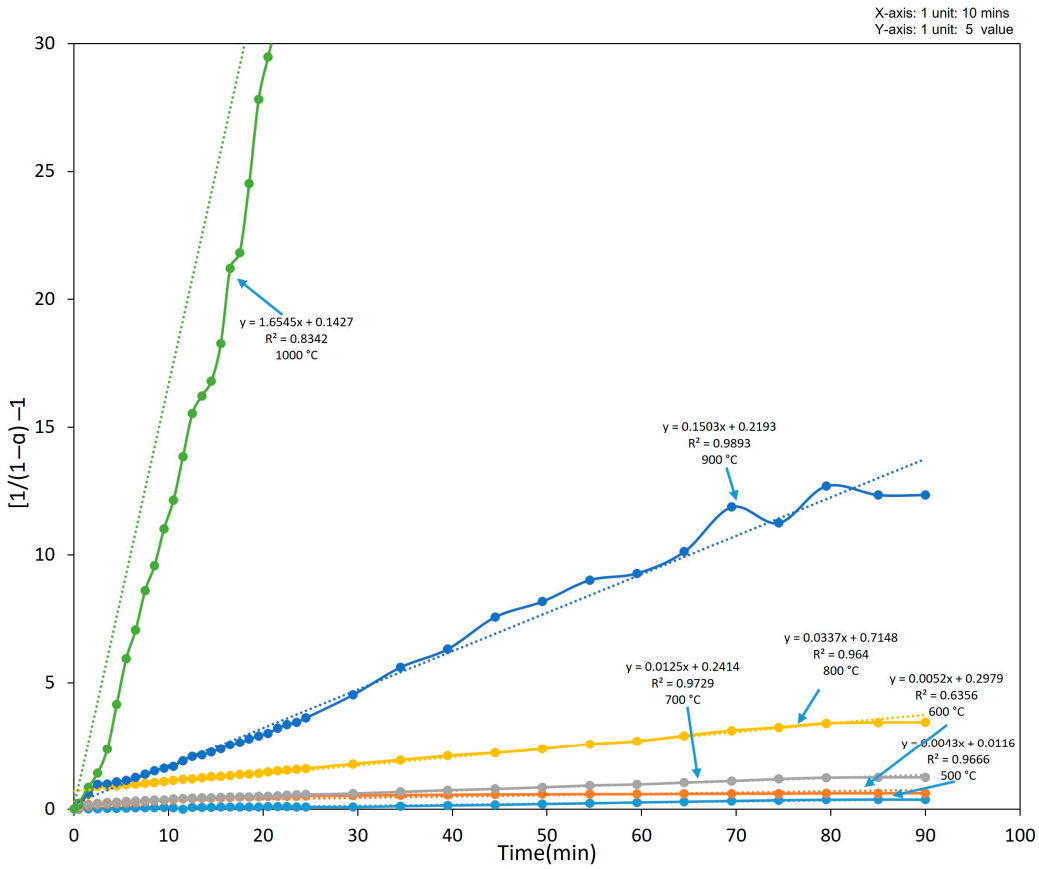

Figure 19. Relation between $[1/(1-\alpha)]-1$ and time for different reduction temperatures.

Table 3. Kinetic models for reduction reaction [24].

Integral Form g(α) = kt	Equation	Model	Activation Energy (kJ/mol)	R^2
$-\ln(1-\alpha) = kt$	(11)	1st Order	55.1	0.93
$[1/(1-\alpha)] - 1 = kt$	(12)	2nd order	96.6	0.91

where α is the fraction reacted, k is the rate constant, and t is the reduction time.

By plotting the right-hand side of Equations (11) and (12) against the reduction time, the activation energy of different models could be obtained. By using the reduction rate constant from every temperature of a particular model, the activation energy was calculated using Equation (13), according to the Arrhenius equation [25]:

$$\ln k_{red} = \ln k - \left(\frac{E_a}{RT}\right) \quad (13)$$

where k_{red} is the reduction rate constant, k is a frequency factor, R is the gas constant, E_a is the apparent activation energy and T is the absolute temperature in kelvin. The $\ln k_{red}$ with respect to 1/T (K) for all order reactions is presented in Figure 20.

Furthermore, by applying Equation (13), the activation energy of the reduction reaction for first-order and second-order models is 55.1 kJ/mol and 96.65 kJ/mol, respectively. However, the second-order reaction changed its slope when moving from lower-temperature to higher-temperature reduction. This change in slope from a lower temperature to a higher reduction temperature may be due to the sintering of particles in the pellet, which results in decreases in the porosity of the pellets at higher temperatures, and it is correlated with the SEM image analysis. Figure 11b–d indicates that with increases in the reduction temperature, there is the gradual sintering of particles. Both the porosity of reduced pellets (Figure 7) and sintering of grains (Figure 11d) could justify the alteration in E_a and change

in the reaction mechanism. In the literature, the activation energy of iron oxide in isothermal reduction by hydrogen is in the range of 47.2–89.9 kJ/mol [18,26] and that for BR pellets reduced with hydrogen with varying temperatures from 700 to 1100 °C is 67.18 kJ/mol [27].

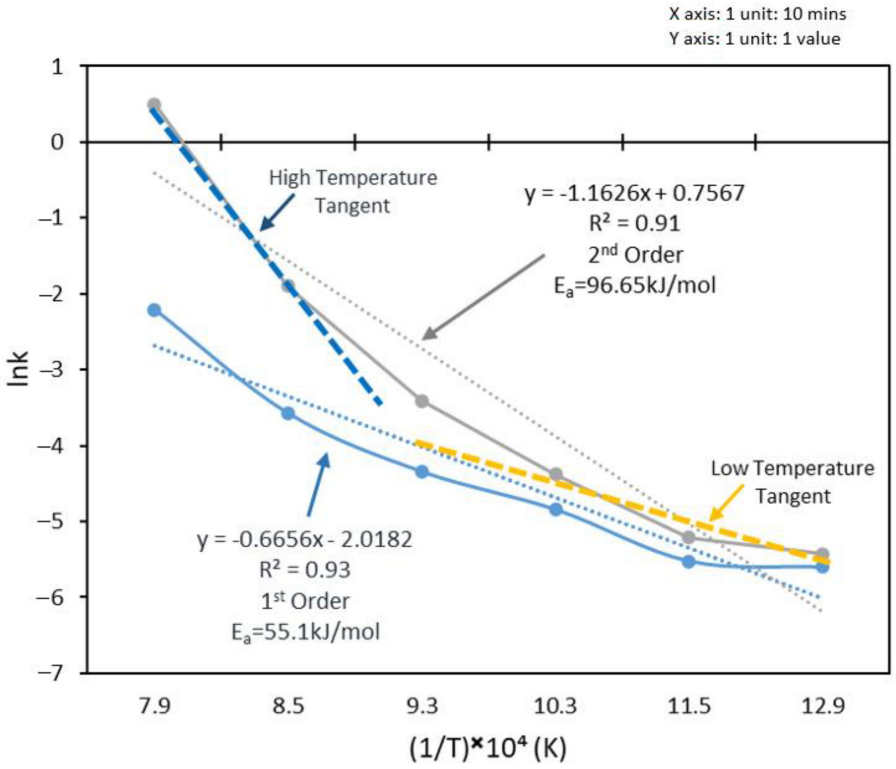

Figure 20. Arrhenius plot of different reaction orders under H_2 reduction.

5. Conclusions

The hydrogen reduction of sintered pellets was studied using thermogravimetry methods under isothermal conditions and by studying the gas flow rate effect. The main conclusions of this work are summarized as follows:

1. At a 1000 °C reduction temperature and 90 min reduction time, the reduction rate was the fastest with a 4 NL/min flow rate of hydrogen.
2. With increases in the reduction temperature, the number of iron oxide complexes decreases and the metallic iron product increases. Reduction reactions occur at the lowest temperature of 500 °C; however, it is slow, with approximately 28% within 120 min.
3. The porosity, density and BET surface area measurements for reduced pellets indicated that at moderate temperatures such as 800 °C, with a high reduction degree, the porosity is the highest, and it is decreased with an increasing temperature due to sintering. However, lower temperatures may yield lower porosity due to the smaller extent of reduction within the same reduction time.
4. The formation of a leachable mayenite phase from brownmillerite during hydrogen reduction is enhanced at temperatures of 900 °C and higher.
5. First-order and second-order kinetics yielded activation energies of 55.1 kJ/mol and 96.6 kJ/mol, respectively. The second-order reaction may describe the effect of sintering at elevated temperatures and suggests that the process may have a different activation energy based on the temperature.

Author Contributions: Conceptualization, M.K.K. and J.S.; methodology, M.K.K. and J.S.; software, M.K.K.; validation, M.K.K., J.S. and C.v.d.E.; formal analysis, M.K.K. and J.S.; investigation, M.K.K. and J.S.; resources, M.K.K., J.S. and C.v.d.E.; data curation, M.K.K. and J.S.; writing—original draft preparation, M.K.K.; writing—review and editing, M.K.K., J.S. and C.v.d.E.; visualization, M.K.K.

and J.S.; supervision, J.S. and C.v.d.E.; project administration, J.S. and C.v.d.E.; funding acquisition, J.S. and C.v.d.E. All authors have read and agreed to the published version of the manuscript.

Funding: This project has received funding from the European Union's Horizon 2020 research and innovation program under grant agreement No. 958307. This publication represents only the authors' views, exempting the community from any liability. The HARARE project website is https://h2020harare.eu/ (accessed on 2 January 2023).

Data Availability Statement: Not applicable.

Conflicts of Interest: The authors declare no conflict of interest.

References

1. Cardenia, C.; Balomenos, E.; Panias, D. Iron Recovery from Bauxite Residue through Reductive Roasting and Wet Magnetic Separation. *J. Sustain. Metall.* **2019**, *5*, 9–19. [CrossRef]
2. Yang, J. Research on Comprehensive Utilization of Red Mud from Alumina Plant. *Huazhong Univ. Sci. Technol. China* **2006**.
3. Evans, K. The History, Challenges, and New Developments in the Management and Use of Bauxite Residue. *J. Sustain. Metall.* **2016**, *2*, 316–331. [CrossRef]
4. Kalkan, E. Utilization of Red Mud as a Stabilization Material for the Preparation of Clay Liners. *Eng. Geol.* **2006**, *87*, 220–229. [CrossRef]
5. Evans, K.; Nordheim, E.; Tsesmelis, K. Bauxite Residue Management. In *Light Metals 2012*; Springer: Berlin/Heidelberg, Germany, 2012; pp. 63–66.
6. Lazou, A.; Van Der Eijk, C.; Tang, K.; Balomenos, E.; Kolbeinsen, L.; Safarian, J. The Utilization of Bauxite Residue with a Calcite-Rich Bauxite Ore in the Pedersen Process for Iron and Alumina Extraction. *Metall. Mater. Trans. B* **2021**, *52*, 1255–1266. [CrossRef]
7. Borra, C.R.; Blanpain, B.; Pontikes, Y.; Binnemans, K.; Van Gerven, T. Smelting of Bauxite Residue (Red Mud) in View of Iron and Selective Rare Earths Recovery. *J. Sustain. Metall.* **2016**, *2*, 28–37. [CrossRef]
8. European Commission: EU Waste Legislation. Available online: https://environment.ec.europa.eu/topics/waste-and-recycling/waste-law_en (accessed on 15 March 2023).
9. Directive, E. Mining Council of the European Union, European Parliament (2006) Directive 2006/21/EC of the European Parliament and of the Council of 15 March 2006 on the Management of Waste from Extractive Industries and Amending Directive 2004/35/EC. Available online: https://eur-lex.europa.eu/legal-content/EN/TXT/?uri=CELEX%3A32006L0021 (accessed on 15 March 2006).
10. Kumar, S.; Kumar, R.; Bandopadhyay, A. Innovative Methodologies for the Utilisation of Wastes from Metallurgical and Allied Industries. *Resour. Conserv. Recycl.* **2006**, *48*, 301–314. [CrossRef]
11. Johansson, A. *Clean Technology*; CRC Press: Boca Raton, FL, USA, 1992; ISBN 0873715039.
12. Souza Filho, I.R.; Springer, H.; Ma, Y.; Mahajan, A.; da Silva, C.C.; Kulse, M.; Raabe, D. Green Steel at Its Crossroads: Hybrid Hydrogen-Based Reduction of Iron Ores. *J. Clean. Prod.* **2022**, *340*, 130805. [CrossRef]
13. Ma, Y.; Souza Filho, I.R.; Bai, Y.; Schenk, J.; Patisson, F.; Beck, A.; van Bokhoven, J.A.; Willinger, M.G.; Li, K.; Xie, D. Hierarchical Nature of Hydrogen-Based Direct Reduction of Iron Oxides. *Scr. Mater.* **2022**, *213*, 114571. [CrossRef]
14. Turkdogan, E.T.; Vinters, J.V. Gaseous Reduction of Iron Oxides: Part I. Reduction of Hematite in Hydrogen. *Metall. Mater. Trans. B* **1971**, *2*, 3175–3188. [CrossRef]
15. El-Geassy, A.A.; Nasr, M.I. Influence of the Original Structure on the Kinetics of Hydrogen Reduction of Hematite Compacts. *Trans. Iron Steel Inst. Jpn.* **1988**, *28*, 650–658. [CrossRef]
16. Kazemi, M.; Pour, M.S.; Sichen, D. Experimental and Modeling Study on Reduction of Hematite Pellets by Hydrogen Gas. *Metall. Mater. Trans. B* **2017**, *48*, 1114–1122. [CrossRef]
17. Paris Agreement. 2015. Available online: https://www.un.org/en/climatechange/net-zero-coalition (accessed on 15 March 2023).
18. Spreitzer, D.; Schenk, J. Reduction of Iron Oxides with Hydrogen—A Review. *Steel Res. Int.* **2019**, *90*, 1900108. [CrossRef]
19. Bhaskar, A.; Assadi, M.; Nikpey Somehsaraei, H. Decarbonization of the Iron and Steel Industry with Direct Reduction of Iron Ore with Green Hydrogen. *Energies* **2020**, *13*, 758. [CrossRef]
20. Jozwiak, W.K.; Kaczmarek, E.; Maniecki, T.P.; Ignaczak, W.; Maniukiewicz, W. Reduction Behavior of Iron Oxides in Hydrogen and Carbon Monoxide Atmospheres. *Appl. Catal. A Gen.* **2007**, *326*, 17–27. [CrossRef]
21. Baolin, H.; ZHANG, H.; Hongzhong, L.I.; Qingshan, Z.H.U. Study on Kinetics of Iron Oxide Reduction by Hydrogen. *Chin. J. Chem. Eng.* **2012**, *20*, 10–17.
22. Kar, M.K.; Safarian, J. Characteristics of Bauxite Residue–Limestone Pellets as Feedstock for Fe and Al_2O_3 Recovery. *Processes* **2023**, *11*, 137. [CrossRef]
23. Kar, M.K.; Van Der Eijk, C.; Safarian, J. Hydrogen Reduction of High Temperature Sintered and Self-Hardened Pellets of Bauxite Residue Produced via the Addition of Limestone and Quicklime. In Proceedings of the 40th International ICSOBA Conference, Athens, Greece, 10–14 October 2022; p. 11.

24. Khawam, A.; Flanagan, D.R. Solid-State Kinetic Models: Basics and Mathematical Fundamentals. *J. Phys. Chem. B* **2006**, *110*, 17315–17328. [CrossRef]
25. Laidler, K.J. The Development of the Arrhenius Equation. *J. Chem. Educ.* **1984**, *61*, 494. [CrossRef]
26. Lee, G.-Y.; Choi, J.-P.; Song, J.-I.; Jung, S.-S.; Lee, J.-S. The Kinetics of Isothermal Hydrogen Reduction of Nanocrystalline Fe_2O_3 Powder. *Mater. Trans.* **2014**, *55*, 1611–1617. [CrossRef]
27. Man, Y.; Feng, J. Effect of Gas Composition on Reduction Behavior in Red Mud and Iron Ore Pellets. *Powder Technol.* **2016**, *301*, 674–678. [CrossRef]